



Temporal-spatial two-dimensional sparse deconvolution beamforming for wideband underwater acoustic multipath signals

Quan Tao, Jingjing Fan, Zhiwen Qian, Xiaomei Fu^{*}

School of Marine Science and Technology, Key Laboratory of Ocean Observation Technology of Ministry of Natural Resources, Tianjin University, Tianjin 300072, PR China

ARTICLE INFO

Keywords:

Array signal processing
Multipath effect
Joint temporal-spatial estimation
Sparse deconvolution

ABSTRACT

Direction-of-arrival (DOA) estimation is crucial for marine applications, but it faces significant challenges in multipath environments where the received signals are often coherent. While several algorithms exist for narrowband signals, they struggle with wideband signals widely used in the active sonar system, especially when these signals are spatially close or overlapping.

To address these issues, a temporal-spatial two-dimensional sparse deconvolution joint estimation algorithm (T-SSD) is proposed in this paper. Firstly, to fully utilize the information of the source signal, we develop a joint time-of-arrival (TOA)-DOA estimation model based on the cross-correlation, so that the output SNR is maximized, and the robustness of wideband beamforming based on matrix transformation is enhanced. Secondly, we design a multipath separation sliding window based on the time-domain Finite-Impulse-Response (FIR) filter, which preliminarily minimizes interference between adjacent paths and gives intermediate TOA-DOA estimations with limited resolution. Finally, a deconvolution algorithm with sparseness and continuity constraints is applied as a post-processor in the joint TOA-DOA estimation model, thereby suppressing the main-lobe width and side-lobe level of the intermediate TOA-DOA estimation, resulting in high-resolution results.

Numerical simulations and underwater experiments validate the effectiveness of T-SSD. The results show that traditional one-dimensional methods for reliable DOA measurement require angular intervals greater than 5°, but T-SSD can handle arbitrary angular intervals with path relative delays over 3 ms. Additionally, T-SSD can maintain satisfying performance even in low signal-to-noise ratio (SNR) and small array aperture, making it more suitable for measurements in practical underwater environments.

1. Introduction

Array signal processing is a key technology in radar and terrestrial communication systems [1–5]. With the development of marine applications, such as sunken ship localization, offshore activities and underwater target identification, underwater direction-of-arrival (DOA) and time-of-arrival (TOA) estimation has become increasingly attractive during the last decade [6,7]. However, the complex underwater channel environment presents greater challenges for accurately estimating these measurement metrics compared to terrestrial settings [8,9]. One common challenge is the noisy environment caused by high propagation loss. Another major challenge is the multipath effect, which causes the source to reach the receiving array through multiple paths, resulting in the signals from different paths becoming coherent. What's worse, if these paths overlap in range/direction units, it is difficult to distinguish

them on the temporal-spatial two-dimensional plane and achieve accurate measurement.

Benefit from its distinguished robustness and low computational complexity, conventional beamforming (CBF) is widely adopted in underwater DOA estimation [10]. However, due to the Rayleigh constraints caused by the small array aperture, CBF results are often blurred with low spatial resolution [11]. Although the resolution can be improved by increasing the array aperture, it significantly increases deployment difficulty and compromises concealment in practical applications [12–14].

In recent years, deconvolution algorithms, originally developed for image restoration, have been applied to post-process CBF results to improve spatial resolution without expanding the array aperture [15–23]. Specifically, the CBF results with limited resolution are considered as a convolution of beam patterns and source intensity

* Corresponding author.

E-mail addresses: TQdidi@tju.edu.cn (Q. Tao), fanjingjing_99@tju.edu.cn (J. Fan), zhiwenqian@tju.edu.cn (Z. Qian), fuxiaomei@tju.edu.cn (X. Fu).

distributions with super resolution. Therefore, deconvolution algorithms attempt to recover the true source distributions from the CBF results to enhance resolution. Based on this idea, Yang successfully applied the Richardson-Lucy (R-L) deconvolution algorithm to CBF with a uniform line array (ULA) [24], and achieved narrower beamwidth and lower side-lobe level. Meanwhile, it retains the robustness of CBF under low signal-to-noise ratio (SNR) environment.

Because of the nonlinear operation in constructing the spectrum convolution response, the above algorithms [15–23] can only handle scenarios where the received signals are incoherent. Their DOA measurement results will be biased due to cross-term side-lobe[25] when directly applied to actual underwater environments. To address this issue, some scholars have developed these algorithms to coherent scenarios[26–28]. Wang utilized the CBF results in complex-valued domain to avoid interference from cross-term side-lobe to perform deconvolution beamforming, and achieved super-resolution estimation for narrowband signals [28].

Recent studies have mainly focused on improving spatial resolution, and there are only a few studies that focused on synthetically enhancing the temporal resolution. In fact, the joint estimation of TOA-DOA usually achieves higher accuracy than single parameter estimation. This is because joint TOA-DOA estimation can fully utilize the correlation and mutual influence between these parameters [29,30].

Typically, the TOA-DOA estimation algorithms are mainly divided into two categories: multi-parameter-estimation-based [31–33] and subspace-based [34,35]. The first type of methods, such as ML [31], EM [32], SAGE [33], involve multidimensional nonlinear optimization and parameter searching problems, which are slow to converge and sensitive to the initialization parameters. The subspace-based methods, such as JADE-ESPRIT [34] and TLS-ESPRIT [35], reduce complexity by eliminating the need for multiple iterations. But they require additional decoherence algorithms for coherent environments and exhibit poor accuracy in low SNR conditions.

However, it is worth noting that the aforementioned joint estimation method [31–33] and deconvolution beamforming [26–28] can only utilize the statistical characteristics of the array receiving signals. In the application of integrated sonar and communication systems, or other collaborative systems that widely use wideband signals, the prior information of source signal waveform can be available. It has been demonstrated that the Cramer-Rao bound (CRB) for DOA estimation is significantly lower for signals with known waveforms compared to those without.

To address the joint TOA-DOA estimation problems for underwater wideband sources with known waveforms, a temporal-spatial two-dimensional sparse deconvolution joint estimation algorithm (T-SSD) is proposed in this paper. The main steps of T-SSD are as follows. Firstly, we utilize a TOA estimation model, where temporal information is obtained from cross-correlation. And then a multipath separation sliding window based on the time-domain Finite-Impulse-Response (FIR) filter is designed to preliminarily minimize interference between multipaths. Secondly, the TOA estimation model is extended to a joint TOA-DOA estimation model. In this model, cross-correlation-based beamforming for wideband signals is proposed by converging these signals to a signal reference frequency through matrix transformation. So, the temporal and spatial information are coupled without additional pairing operations, and the output SNR is maximized. Finally, a two-step deconvolution algorithm with sparseness and continuity constraints is proposed to mitigate cross-term side-lobe and compress the width of the main-lobe. Hence, the temporal and spatial resolution of T-SSD is sufficiently high to distinguish underwater multipath signals with very close TOA or DOA.

The main contributions of this paper are summarized as follows:

- (1) A joint TOA-DOA estimation model is developed from the existing TOA estimation model, where cross-correlation-based beamforming for wideband signals is proposed. Due to the full

utilization of prior waveform information, the new model maximizes the output SNR and couples temporal and spatial information without additional pairing operations. However, the estimation resolution of this model is limited by signal bandwidth in the temporal domain and Rayleigh constraints in the spatial domain.

- (2) T-SSD is proposed to improve the resolution of TOA-DOA estimations. The Fast Iterative Shrinkage-Thresholding Algorithm (FISTA) with sparseness and continuity constraints is applied in complex-valued to mitigate cross-term side-lobe caused by the nonlinear operation in constructing the spectrum convolution response in the spatial domain, and (R-L) deconvolution algorithm is then applied to compress the main-lobe width in the temporal domain.

Numerical simulations and underwater experiments were conducted to verify the effectiveness of T-SSD. Its performance was evaluated against other one-dimensional or joint estimation algorithms under various SNR conditions, with the CRB introduced as a benchmark for comparison.

The rest of this paper is composed as follows. Section 2 describes the array receiving signal model in a multipath environment. Section 3 describes deconvolution models in spatial and temporal domain and proposes T-SSD with FISTA and R-L. Sections 4 and 5 show the performance of T-SSD through numerical simulations and underwater experiments. Finally, Section 6 concludes the paper and makes an expectation.

Notations: in subsequent sections, vectors and matrices are denoted by lower-case and bold capital letters, respectively. $(\cdot)^T$, $(\cdot)^H$, $(\cdot)^*$ and (\otimes) stand for transpose, conjugate transpose, complex conjugate and convolution, respectively.

2. Array multipath signal model

In the array multipath signal model, three conventional assumptions are made. Firstly, assuming the source is a point source, and the channel remains stable during propagation. Consequently, the multipaths between the source and the reference array element are similar to those between the source and the array. Secondly, assuming all the multipaths come from the far field, this guarantees that the wavefront reaching the array is a plane wave [36,37]. Thirdly, assuming that only a limited number of multipath can be transmitted in the underwater acoustic channel [38], this highlights the sparsity of the channel.

We consider a ULA consisting of M isotropic hydrophones and use the first hydrophone as the reference array element. As shown in the left half of Fig. 1, there are L propagation paths reaching the array, with DOA θ_l defined as the angle between the l -th ($l = 1, 2, \dots, L$) path and the normal direction of the array, and with TOA t_l defined as the transmission time of the l -th path wave from the transmitter to the reference array element. As shown in the right half of Fig. 1, the relative delay for the l -th path from the reference array element to the m -th ($m = 1, 2, \dots, M$) array element is expressed as:

$$\tau_{m,l} = \frac{(m-1)d\sin\theta_l}{c} \quad (1)$$

where d is the distance between adjacent array elements, and c is the sound speed in water.

The corresponding steering vector is

$$\begin{aligned} v_r &= [v_{r1}, \dots, v_{rm}, \dots, v_{rM}]^T \\ v_{rm}(\theta, t) &= e^{-j2\pi f(t)\tau_{m,l}(\theta)} \end{aligned} \quad (2)$$

The hydroacoustic multipath channel impulse response model of the m -th array element can be expressed as:

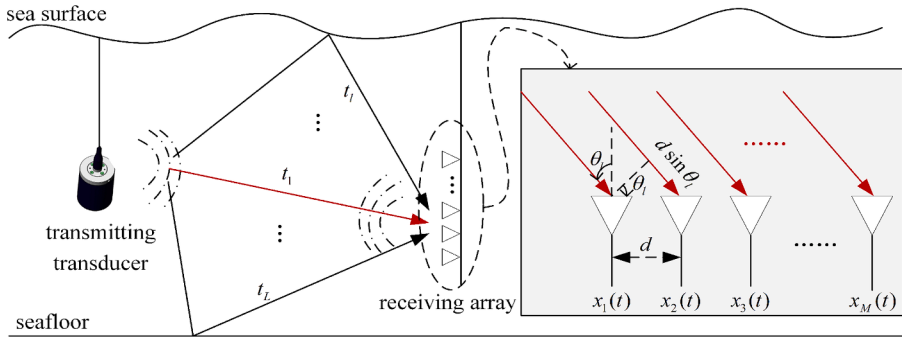


Fig. 1. Array signal model in a multipath environment.

$$h_m(t) = \sum_{l=1}^L \beta_l \delta(t - t_l - \tau_{m,l}) \quad (3)$$

where β_l is the attenuation of the l -th path.

The received signal of the m -th array element $x_m(t)$ is expressed as:

$$\begin{aligned} x_m(t) &= h_m(t) \otimes s_0(t) \\ &= \sum_{l=1}^L \beta_l s_0(t - t_l - \tau_{m,l}) + z_m(t) \\ &= \sum_{l=1}^L \beta_l s_{m,l}(t) + z_m(t) \end{aligned} \quad (4)$$

where $s_0(t)$ is the source signal, $s_{m,l}(t)$ denotes the l -th path signal received by m -th array element, $z_m(t)$ represents a white Gaussian noise vector and is not correlated with the source $s_0(t)$.

Hence, the array signal model in multipath environments can be represented in matrix form as follows:

$$\mathbf{X}(t) = \mathbf{H}(t) \otimes s_0(t) + \mathbf{Z}(t) \quad (5)$$

where $\mathbf{X}(t) = [x_1(t), x_2(t), \dots, x_M(t)]^T$ represents the array receiving signal, $\mathbf{H}(t) = [h_1(t), h_2(t), \dots, h_M(t)]^T$ represents the hydroacoustic multipath channel impulse response matrix, $\mathbf{Z}(t) = [z_1(t), z_2(t), \dots, z_M(t)]^T$ represents a white Gaussian noise matrix.

3. The proposed algorithm T-SSD

This section proposes T-SSD for wideband sources. In T-SSD, temporal information can not only improve spatial resolution, but also provide another criterion for multipath classification. First, the temporal information is coupled with the spatial information to construct a joint TOA-DOA estimation model based on cross-correlation. Second, the joint estimation model is transformed into two dimensions and post-processed by a deconvolution algorithm with sparseness and continuity constraints to suppress the main-lobe width and the side-lobe level, thus TOA-DOA estimations with high resolution can be obtained.

3.1. Joint TOA-DOA estimation model

In the application of integrated sonar and communication system, the linear frequency modulation (LFM) source signal can be expressed as

$$s_0(t) = \sigma_s e^{j2\pi\alpha t + j\pi\beta t^2}, 0 \leq t \leq T \quad (6)$$

Where σ_s is the signal amplitude, α is the starting frequency, β is the chirp rate, and T is the signal time duration.

The steering vector of LFM signal is

$$\begin{aligned} v_r^1 &= [v_{r1}^1, \dots, v_{rm}^1, \dots, v_{rM}^1]^T \\ v_{rm}^1(\theta, t) &= e^{-j2\pi\tau_{m,l}(\theta)} \left[f_0 + \beta(t - t_l) - \frac{\beta}{2}\tau_{m,l}(\theta) \right] \end{aligned} \quad (7)$$

The steering vector v_r^1 depends not only on angle but also on the path transmission time t_l and the chirp parameters. So, we need to estimate the TOA before estimating DOA. But it is worth noting that TOA estimation errors will affect the DOA estimation process.

To eliminate this impact, we develop the array signal model with a cross-correlation process, which can be expressed as:

$$\begin{aligned} \mathbf{R}_{xs}(t) &= \mathbf{X}(t) \otimes s_0(-t) \\ &= \mathbf{H}(t) \otimes s_0(t) \otimes s_0(-t) + \mathbf{Z}(t) \otimes s_0(-t) \\ &= \mathbf{H}(t) \otimes R_{ss}(t) + \mathbf{Z}(t) \otimes s_0(-t), \end{aligned} \quad (8)$$

where $\mathbf{R}_{xs}(t) = [R_{x_1s}, \dots, R_{x_ms}, \dots, R_{xMs}]^T$, R_{x_ms} denotes the cross-correlation result of the m -th array element. If the noise term is ignored, it shows the cross-correlation matrix $\mathbf{R}_{xs}(t)$ can be expressed as the convolution of the source signal auto-correlation $R_{ss}(t)$ with the channel $\mathbf{H}(t)$.

Next, we demonstrate that the cross-correlation matrix $\mathbf{R}_{xs}(t)$ contains not only temporal information but also spatial information. The cross-correlation result R_{x_ms} can be expressed as

$$\begin{aligned} R_{x_ms} &= x_m(t) \otimes s_0(-t) \\ &= \sum_{l=1}^L \beta_l \delta(t - t_l - \tau_{m,l}) \otimes s_0(t) \otimes s_0(-t) + z_m(t) \otimes s_0(-t) \\ &= \sum_{l=1}^L \beta_l s(t - t_l - \tau_{m,l}) \otimes s_0(-t) + z_m(t) \otimes s_0(-t) \\ &= \sum_{l=1}^L \int_0^{f_s} \beta_l \left[S_l(f) e^{-j2\pi f(t_l + \tau_{m,l})} \right] \left[S_0^*(f) e^{j2\pi f t} \right] df + \eta_m(t) \\ &= \sum_{l=1}^L \int_0^{f_s} \beta_l \left[S_l(f) S_0^*(f) e^{-j2\pi f[t - (t_l + \tau_{m,l})]} \right] df + \eta_m(t) \\ &= \sum_{l=1}^L f_s |\sigma_l| |\sigma_s| e^{-j2\pi f_c^l [t - (t_l + \tau_{m,l})]} \text{sinc} \{ f_s [t - (t_l + \tau_{m,l})] \} + \eta_m(t) \end{aligned} \quad (9)$$

Where $\text{sinc}(\cdot)$ is the sinc function; f_s is the sampling frequency; $s_0(t)$ is the normalized original wide-band chirp signal; and $S_l(f) e^{-j2\pi f(t_l + \tau_{m,l})}$ and $S_0^*(f)$ are the FT of $s(t - t_l - \tau_{m,l})$ and $s_0(t)$, respectively. The center frequency of the l -th path signal f_c^l can be accurately estimated by calculating the spectral centroid of R_{x_ms} .

$$\hat{f}_c^l = \frac{\int_0^{f_s} f \cdot |X_m(f) S_l^*(f)| df}{\int_0^{f_s} |X_m(f) S_l^*(f)| df} \quad (10)$$

Where the spectral centroid is the center of gravity of the spectrum. Cross-correlation process compresses the signal, yields significant

peaks, and maximizes output SNR, resulting in robust performance of the proposed scheme. The corresponding derivation is given in Appendix A.

In (9), the energy of $R_{x_m s}$ is concentrated at $t_l + \tau_{ml}$ in the time domain. The maximum value of $R_{x_m s}$ is found at time index \hat{t}_l as follows:

$$\hat{t}_l = \frac{1}{M} \sum_{M=1}^M \operatorname{argmax}_t \{|R_{x_m s}|_t\} \quad (11)$$

The value of $R_{x_m s}$ at \hat{t}_l can then be expressed as

$$\begin{aligned} R_{x_m s}(\hat{t}_l) &= \sum_{l=1}^L f_s |\sigma_l| |\sigma_s| e^{j2\pi f_c^l [(\hat{t}_l - t_l) + \tau_{ml}]} \\ &\times \operatorname{sinc}\{f_s[(\hat{t}_l - t_l) + \tau_{ml}]\} + \eta_m(t) \\ &\approx \sum_{l=1}^L f_s |\sigma_l| |\sigma_s| e^{j2\pi f_c^l (\tau_{ml})} + \eta_m(t) \end{aligned} \quad (12)$$

$$\operatorname{sinc}\{\hat{f}_s[(\hat{t}_l - t_l) + \tau_{ml}]\} \approx 1$$

To preliminarily minimize interference between these significant peaks revealing TOA information, rectangular windows are used because of its linear phase frequency characteristics[39]. The rectangular window function $G_{win}(y)$ is defined as:

$$G_{win}(y) = \begin{cases} 1, & \text{win}_{start} \leq y \leq \text{win}_{end}, \\ 0, & \text{else} \end{cases} \quad (13)$$

where win_{start} and win_{end} are the left and right endpoint of the rectangular window, the window length is $|\text{win}_{end} - \text{win}_{start}|$.

Within the same sliding window, these peaks may not be distinguished from each other with high confidence. After all, in practical applications, the paths may arrive at the array at the same time. Therefore, TOA model is developed to TOA-DOA model with CBF implement to distinguish these paths in spatial domain.

Based on formula (9)(12), it has

$$R_{x_m s} = R_{x_1 s} \cdot v_r^0(\theta) = R_{x_1 s} e^{-j2\pi f_c^l \tau_{ml}} \quad (14)$$

Different from the time-varying steering vector v_r^1 , the cross-correlation-based steering vector $v_r^0 = [v_{r1}^0, \dots, v_{rm}^0, \dots, v_{rM}^0]^T$ depends only on the unknown multipath DOA. Thus, the DOA estimation can be

wideband source in the multipath environment as:

$$\begin{aligned} P_{\theta-\tau} &= (v_r^0)^H \mathbf{R}_{narrow} v_r^0 \\ &= \frac{1}{M^2} \left(e^{\frac{j2\pi f_0(m-1)d\sin\theta_r}{c}} \right)^H \mathbf{R}_{narrow} \left(e^{\frac{j2\pi f_0(m-1)d\sin\theta_r}{c}} \right) \end{aligned} \quad (16)$$

where f_0 denotes the reference frequency. The derivation of how to transform the covariance matrix to the reference frequency is given in Appendix B&C.

The specific flow is shown in Fig. 2. Firstly, the source signal reaches the hydrophone array through different paths, as shown in (5). Secondly, the received signals are cross-correlated with the source signal $s_0(t)$, and then the cross-correlation results $R_{x_m s}$ are divided into P overlapped sliding windows according to the distribution of temporal peaks. Finally, cross-correlation-based CBF is performed in each sliding window based on the steering vector $v_{rm}^0(t)$.

By constructing the above model, joint TOA-DOA estimation results of multipath signals can be obtained simultaneously without additional pairing operations. Moreover, the interference between different paths can be minimized, and the output SNR can be improved. However, the resolution of obtained Temporal-Spatial 2D raw map is limited by signal bandwidth and Rayleigh constraints. In the next part, a post-processing method based on deconvolution algorithm with sparseness and continuity constraints will be introduced to improve the resolution.

3.2. Cross-correlation-based deconvolution model

In the temporal domain, the normal convolution model shown as formula (4) is among the source signal $s(t)$, the hydroacoustic multipath channel impulse response $h_m(t)$ and the received signal $x_m(t)$. While the cross-correlation-based convolution model shown as formula (8) is among the auto-correlation of source signal $R_{ss}(t)$, the hydroacoustic multipath channel impulse response $h_m(t)$ and the cross-correlation vector $R_{xs}(t)$. And this relation can be represented by the following matrix multiplication:

$$\mathbf{w}_{time} q_{time} = b_{time} \quad (17)$$

where $|H(t)|$ and $|R_{xs}(t)|$ are the elements in q_{time} and b_{time} , respectively. The discrete form of \mathbf{w}_{time} is expressed as:

$$\mathbf{w}_{time} = \begin{bmatrix} |R_{x_1 s}(-Q - \tau_1)| & |R_{x_1 s}(-Q - \tau_2)| & \dots & |R_{x_1 s}(-Q - \tau_Q)| \\ |R_{x_2 s}(-Q + 1 - \tau_1)| & |R_{x_2 s}(-Q + 1 - \tau_2)| & \dots & |R_{x_2 s}(-Q + 1 - \tau_Q)| \\ \vdots & \vdots & \ddots & \vdots \\ |R_{x_M s}(Q - \tau_1)| & |R_{x_M s}(Q - \tau_2)| & \dots & |R_{x_M s}(Q - \tau_Q)| \end{bmatrix} \quad (18)$$

carried out without estimating TOA. This means that temporal and spatial information have been decoupled, and their errors will not be transmitted to each other.

The joint TOA-DOA estimation model, where cross-correlation-based CBF is performed with temporal peaks data in the same sliding window, is expressed as:

$$\begin{aligned} P_{\theta-\tau} &= \left| (v_r^0)^H \mathbf{X} \otimes s_0 \right|^2 \\ &= \left[(v_r^0)^H \mathbf{X} \otimes s_0 \right] \left[(\mathbf{X} \otimes s_0)^H v_r^0 \right] \\ &= (v_r^0)^H \mathbf{R}_{xs} (\mathbf{R}_{xs})^H v_r^0 \end{aligned} \quad (15)$$

The cross-correlation-covariance matrix $\mathbf{R} = \mathbf{R}_{xs} (\mathbf{R}_{xs})^H$ contains the temporal information, and the steering vector v_r^0 contains spatial information. Therefore, joint TOA-DOA estimation can be obtained from $P_{\theta-\tau}$.

Rewrite (15) to obtain the Temporal-Spatial 2D raw map of the

where $Q = |\text{win}_{end} - \text{win}_{start}|$ is the length of sliding window, $[\tau_1, \tau_1, \dots, \tau_Q]$ is the traversal for the possible transmission time of the multipath. Regardless of whether the signal is coherent or not, this cross-correlation-based convolution model satisfies non-negative constraints. Hence, the deconvolution algorithms can be applied to recover TOA [38,40–42] to improve resolution.

In the spatial domain, the cross-correlation-based beamforming intensity in the desired direction $\theta_r \in (-\pi/2, \pi/2)$ can be expressed as follows:

$$\begin{aligned}
B(\sin\theta_r) &= (\mathbf{v}_r^0)^H \mathbf{R}_{xs} \\
&= \sum_{l=1}^L \frac{f_s |\sigma_l| |\sigma_s|}{M} \sum_{m=1}^M e^{j2\pi(m-1)d(\sin\theta_r - \sin\theta_l)/\lambda_0} \operatorname{sinc}\{f_s [t - (t_l + \tau_{m,l})]\} \\
&\approx \sum_{l=1}^L \frac{f_s |\sigma_l| |\sigma_s|}{M} e^{j2\pi(m-1)d\sin\theta_r/\lambda_0} \frac{\operatorname{sinc}(M\pi d u_{rl}/\lambda_0)}{\operatorname{sinc}(\pi d u_{rl}/\lambda_0)}
\end{aligned} \tag{19}$$

where $u_{rl} = \sin\theta_r - \sin\theta_l/\lambda_0$ is reference wavelength. Clearly, $B(\sin\theta_r)$ can be regarded as the superposition of L propagation paths in the direction θ_r through the beam pattern in the complex-valued domain.

In the complex-valued domain, the cross-correlation-based beamforming intensity of the desired direction θ_r is:

$$\begin{aligned}
B(\sin\theta_r) &= \int_{-1}^1 B_{psf}(\sin\theta_r - \sin\theta) S_p(\sin\theta) d\sin\theta \\
&= B_{psf}(\sin\theta_r) \otimes S_p(\sin\theta_r)
\end{aligned} \tag{20}$$

The expression of the beam pattern is:

$$B_{psf}(\theta_r) = \frac{\operatorname{sinc}(M\pi d\theta_r/\lambda)}{\operatorname{sinc}(\pi d\theta_r/\lambda)} \tag{21}$$

and the source intensity distribution is given by the $S_p(\sin\theta_r) = \sum_{l=1}^L |s_l|^2 \delta(\sin\theta_r - \sin\theta_l)$.

Generally, it is also possible to express the process in (20) through the matrix multiplication in (22).

$$\mathbf{w}_{spa} q_{spa} = b_{spa} \tag{22}$$

where $B_p(\sin\theta_r)$ and $S_p(\sin\theta_r)$ can be regarded as the elements in b_{spa} and q_{spa} respectively. And \mathbf{w}_{spa} is a square matrix, with each column corresponding to a beam pattern in a certain direction θ :

$$\mathbf{w}_{spa} = \begin{bmatrix} B_{psf}(\sin\theta_1 - \sin\theta_1) & B_{psf}(\sin\theta_1 - \sin\theta_2) & \dots & B_{psf}(\sin\theta_1 - \sin\theta_N) \\ B_{psf}(\sin\theta_2 - \sin\theta_1) & B_{psf}(\sin\theta_2 - \sin\theta_2) & \ddots & B_{psf}(\sin\theta_2 - \sin\theta_N) \\ \vdots & \vdots & \ddots & \vdots \\ B_{psf}(\sin\theta_N - \sin\theta_1) & B_{psf}(\sin\theta_N - \sin\theta_2) & \dots & B_{psf}(\sin\theta_N - \sin\theta_N) \end{bmatrix} \tag{23}$$

where $\theta = [\theta_1, \theta_2, \dots, \theta_N] \in (-\pi/2, \pi/2)$ is the traversal of the possible DOA, N is the beam number. When selecting the value of N , there is a trade-off between estimation accuracy and computational complexity. A smaller N may result in lower accuracy, while a larger N will increase the complexity.

Some literature establishes [24,43] the convolutional model from the spectral domain rather than the complex-valued domain, introducing nonlinear errors in coherent scenes.

The cross-correlation-based beamforming spectrum can be expressed as follows:

$$\begin{aligned}
B_p(\sin\theta_r) &= |B(\sin\theta_r)|^2 \\
&= \sum_{l=1}^L |s_l|^2 \left| \frac{\operatorname{sinc}(M\pi d u_{rl}/\lambda_0)}{\operatorname{sinc}(\pi d u_{rl}/\lambda_0)} \right|^2 + \sum_{l=1}^L \sum_{i=1, i \neq l}^L C S_{rl}, \\
&\approx \sum_{l=1}^L |s_l|^2 \left| \frac{\operatorname{sinc}(M\pi d u_{rl}/\lambda_0)}{\operatorname{sinc}(\pi d u_{rl}/\lambda_0)} \right|^2
\end{aligned} \tag{24}$$

It is worth noting that only when the signal incident is incoherent ($s_i s_i^* = 0$) can the sum of the cross-terms $C S_{rl}$ be neglected.

$$C S_{rl} = s_l s_l^* e^{\frac{j\pi(m-1)d u_{rl}}{\lambda}} \frac{\operatorname{sinc}(M\pi d u_{rl}/\lambda_0)}{\operatorname{sinc}(\pi d u_{rl}/\lambda_0)} \times \frac{\operatorname{sinc}(M\pi d u_{rl}/\lambda_0)}{\operatorname{sinc}(\pi d u_{rl}/\lambda_0)}. \tag{25}$$

Then, the beamforming spectrum in (24) can be written as the convolution between the beam pattern $\left| \frac{\operatorname{sinc}(M\pi d u_{rl}/\lambda_0)}{\operatorname{sinc}(\pi d u_{rl}/\lambda_0)} \right|^2$ and the source intensity distribution $|s|^2$.

3.3. Temporal-Spatial 2D sparse deconvolution Post-Processing algorithm

From the above derivation, the cross-correlation-based deconvolution models in temporal and spatial domain are $\mathbf{w}_{spa} q_{spa} = b_{spa}$ and $\mathbf{w}_{time} q_{time} = b_{time}$, respectively. Only a limited number of multipaths can reach the array. Consequently, the number of multipath is much less than the beam number N and the potential transmission delays number Q , making both q_{spa} and q_{time} are sparse.

The deconvolution algorithm with the ℓ_1 -norm sparse constraints to enhance the 2D raw map is expressed as:

$$\text{minimize } \|q\|_1 \text{ subject to } b = \mathbf{W}q. \tag{26}$$

where $b = b_{spa-time}$ is the joint TOA-DOA estimation results in the 2D raw map, $q = q_{spa-time}$ is true source distribution to be recovered, $\mathbf{W} = \{\mathbf{w}_{spa}, \mathbf{w}_{time}\}$ is the dictionary matrix, whose specific expressions are given in (23) and (18).

Normally, the target function (26) is equivalent to the following expression:

$$f(x) = \frac{1}{2} \| \mathbf{W}q - b \|_F^2 + \eta \| \mathbf{D}q \|_1, \tag{27}$$

where $\|\bullet\|_F$ denotes the Frobenius norm. η denotes the regularization coefficient. The value of η is not sensitive to the true source distribution and is generally considered as the mean signal power [44].

Residual waves of $B_{psf}(\theta_r)$ on both sides cause a ringing phenomenon

on the estimation map, seen as oscillations between adjacent grids due to sharp power changes. and the residual waves on both sides will produce the ringing phenomenon on the estimation map. To deal with this challenge, we introduce the difference matrix \mathbf{D} to limit power variation between grids to obtain a smooth beamforming map [45]. \mathbf{D} is generally expressed as a first-order difference matrix:

$$\mathbf{D} = \begin{bmatrix} 1 & -1 & 0 & \dots & 0 \\ 0 & 1 & -1 & \ddots & \vdots \\ 0 & \ddots & \ddots & \ddots & 0 \\ \vdots & \ddots & \ddots & 1 & -1 \\ 0 & \dots & \dots & 0 & 1 \end{bmatrix}. \tag{28}$$

As for the non-negative convex optimization problem (27), it can be solved by using FISTA[19]. In FISTA, general value of a Lipschitz constant for ∇f (denoted as γ) is the maximum eigenvalue of the Hessian matrix $\nabla^2 \Psi = \mathbf{W}^T \mathbf{W}$ [46], where $\Psi(q) = \frac{1}{2} \| \mathbf{W}q - b \|_F^2$.

The gradient of (27) can be expressed as:

$$\nabla f(q) = \mathbf{W}^T (\mathbf{W}q - b) + \eta \mathbf{D}^T \operatorname{sign}(\mathbf{D}q). \tag{29}$$

where $\operatorname{sign}(\bullet)$ is the sign function, i.e., $\operatorname{sign}(x) = \begin{cases} 1, & x > 0 \\ 0, & x = 0 \\ -1, & x < 0 \end{cases}$. Set the

initial value of the vector $Y^{(1)}$ as b , the number of iterations is k , and the iterative process is as follows:

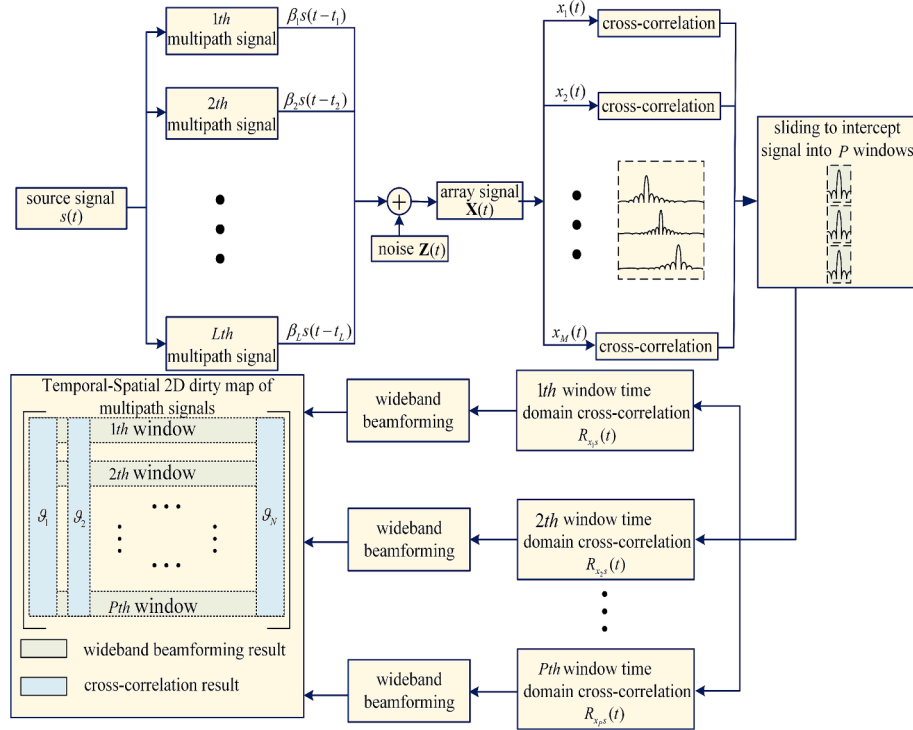


Fig. 2. Joint TOA-DOA estimation model flow chart.

- 1) Update $q_1^{(k)}$: $q_1^{(k)} = \max\left(Y^{(k)} - \frac{1}{\gamma} \nabla f(Y^{(k)}), 0\right)$;
- 2) Update $\beta^{(k+1)}$: $\beta^{(k+1)} = \frac{1 + \sqrt{1 + 4\beta^{(k)}}^2}{2}$;
- 3) Update $Y^{(k+1)}$: $Y^{(k+1)} = q_1^{(k)} + \frac{\beta^{(k)}}{\beta^{(k+1)}} (q_1^{(k)} - q_1^{(k-1)})$.

The FISTA algorithm conducts the above iterative process until $\|q_1^{(k+1)} - q_1^{(k)}\|_F \leq \text{emax}(\|q_1^{(k)}\|_F, 1)$ or k reaches the maximum number of iterations, where the stopping threshold ε is suggested to be selected from 10^{-5} to 10^{-10} .

So far, the cross-term side-lobe has been suppressed by the FISTA algorithm in complex-valued domain. Following the idea in [47], to further reduce the main-lobe width, the R-L algorithm[24] is also performed to ensure q_1^* has as few non-zero elements as possible. The iteration can be expressed as:

$$q_2^{(k+1)} = \frac{1}{a} q_2^{(k)} \left[\mathbf{W}^T \frac{q_1^*}{\mathbf{W} q_2^{(k)}} \right], \quad (30)$$

where k is the number of iterations, the iteration stops when k reaches the maximum number, and the $q_2^{(1)}$ initial value is set to $\frac{1}{a} q_1^*$. In practice,

we generally normalize the received signals, which implies $a \equiv 1$ [16].

Table 1 summarizes the detailed steps of the Temporal-Spatial 2D Sparse deconvolution post-processing algorithm, Fig. 3 shows the corresponding flow chart.

Fig. 3 shows that we first scan each row of $P_{\theta-\tau}$ and apply deconvolution algorithm with sparseness and continuity constraints by using equations (26)-(30). The convolution kernel is the beam pattern obtained from equation (23) in the spatial domain. Similarly, we scan each column of the spatial domain sparse deconvolution result and apply deconvolution algorithm with (26)-(30) in temporal domain. The convolution kernel is the autocorrelation of the source signal R_{ss} . After the above process, the temporal-spatial 2D deconvoluted map is obtained, where the joint TOA-DOA estimation results can be estimated with high resolution by finding the distinct peaks.

4. Simulation

In this section, the performance of T-SSD is verified. Unless otherwise specified, the array comprises eight omnidirectional hydrophones at half-wavelength intervals. The beam pattern in the spatial domain satisfies the shift-invariant property when it is a sine function of the DOA,

Table 1
Proposed measurement scheme.

Algorithm 1: Temporal-Spatial 2D Sparse deconvolution post-processing algorithm.

- Input:** Temporal-Spatial 2D raw map, $P_{\theta-\tau}$
Output: DOAs $\hat{\theta}_l$ and TOAs \hat{t}_l , $l = 1, 2, \dots, L$ estimation of multipath signals
1. Scan each row in the $P_{\theta-\tau}$, i.e., the cross-correlation-based beamforming results for sliding windows;
 2. Calculate sparse dictionary matrix in spatial domain \mathbf{W}_{spa} by (23);
 3. Sparse representation of (26) to a non-negative convex optimization problem by iteratively solving (27) to obtain the sparse map q_1^* ;
 4. Set the corresponding initial value and maximum number of iterations, and repeat the iterative process in (30) to obtain q_2^* ;
 5. Make sparse deconvolution results in spatial domain by $P_{spa} = q_2^*$;
 6. Scan each column in the P_{spa} , i.e., the cross-correlation results for different degrees;
 7. Calculate the time-domain sparse dictionary matrix \mathbf{W}_{time} by (18);
 8. Repeat steps 3 and 4 to obtain P_{T-SSD} after time-domain sparse deconvolution;
 9. Search peaks in P_{T-SSD} for DOA and TOA estimation $\hat{\theta}_l$ and \hat{t}_l .

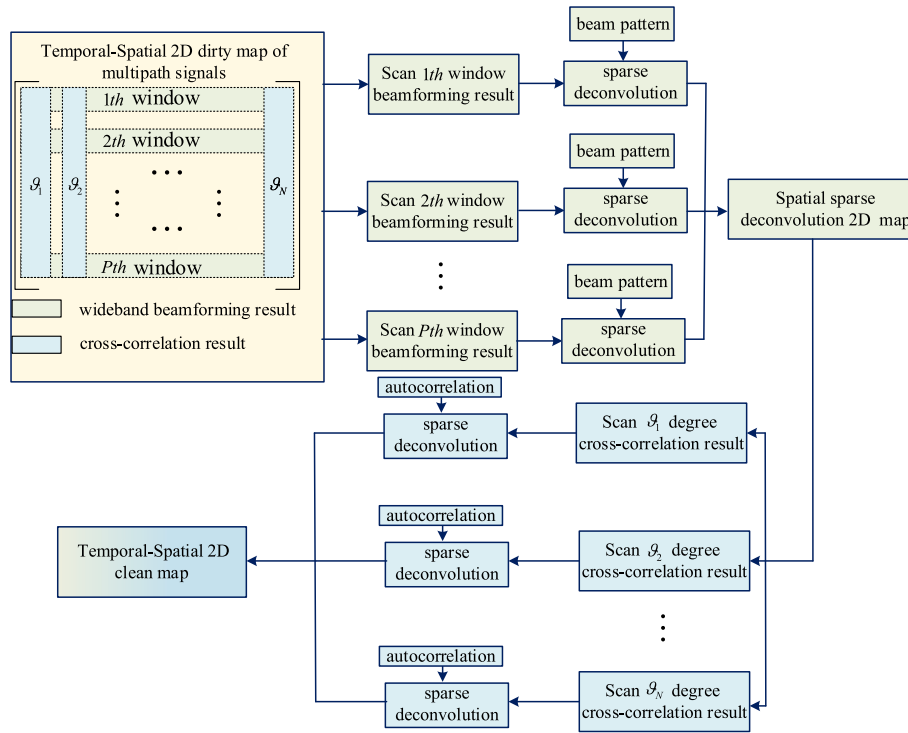


Fig. 3. Temporal-spatial 2D sparse deconvolution (T-SSD) post-processing flow chart.

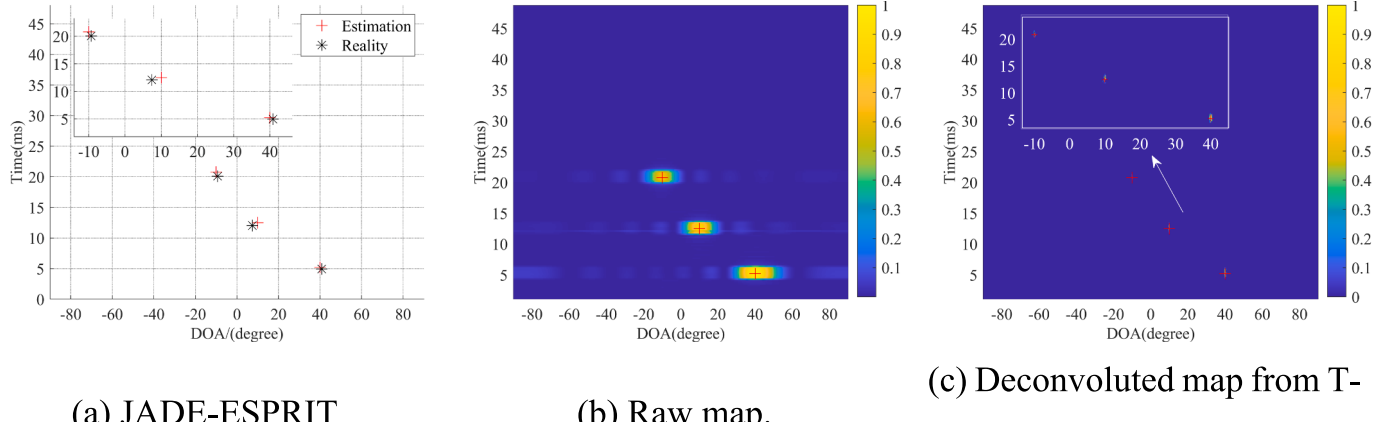


Fig. 4. Distribution of temporal-spatial 2D estimation results at 20 dB.

so the beam sweep range is from -1 to 1 with an increment of 0.001 . Similarly, the source signal auto-correlation function also satisfies the shift-invariant property in the temporal domain. The rectangular window length is chosen to be $3\text{--}6$ times the main-lobe width of the auto-correlation function, and the overlap is set to $70\%\text{--}90\%$. The source signal is an LFM signal with a frequency range of $6\text{--}9$ kHz, a signal length of 50 ms, and a sampling rate of 96 kHz.

4.1. Performance comparison in the case of distant TOA/DOA units

In the first simulation, we consider the LFM source reaching the array along three paths from DOA $[40^\circ, 10^\circ, -10^\circ]$ and TOA $[5.2 \text{ ms}, 12.5 \text{ ms}, 20.8 \text{ ms}]$ with SNR from 20 dB to -10 dB. The performance of T-TSD is compared with the joint subspace-based estimation method JADE-ESPRIT [34].

From Fig. 4(a), (b) and (c), both JADE-ESPRIT, raw map and T-SSD

exhibit slight deviation in TOA and DOA estimation at 20 dB. While it can be seen from Fig. 5(a) that JADE-ESPRIT shows a larger deviation at -10 dB, because of its unreliable estimation of underwater channel at low SNR. Fig. 5(b) and (c) show the effectiveness of the joint estimation model under the same conditions. Comparing Fig. 4(b), (c) or Fig. 5(b), (c), the raw map has a wider main-lobe in both spatial and temporal domain. In addition, two bright spots appear near $[5.2 \text{ ms}, 18^\circ]$ and $[12.5 \text{ ms}, -10^\circ]$ in Fig. 5(b), which are close to the setting distribution at $[20.8 \text{ ms}, -10^\circ]$. Hence, the confidence and readability of Fig. 5(b) is poor because these high side-lobe levels can be easily misunderstood as the setting distribution. In contrast, the deconvoluted map from T-SSD in Fig. 5(c) not only has a narrower main-lobe, but also successfully suppresses the side-lobe level to infinitely close to 0 after normalization. Thus, T-SSD demonstrates the ability to accurately estimate the TOA and DOA of wideband signal in the multipath environment.

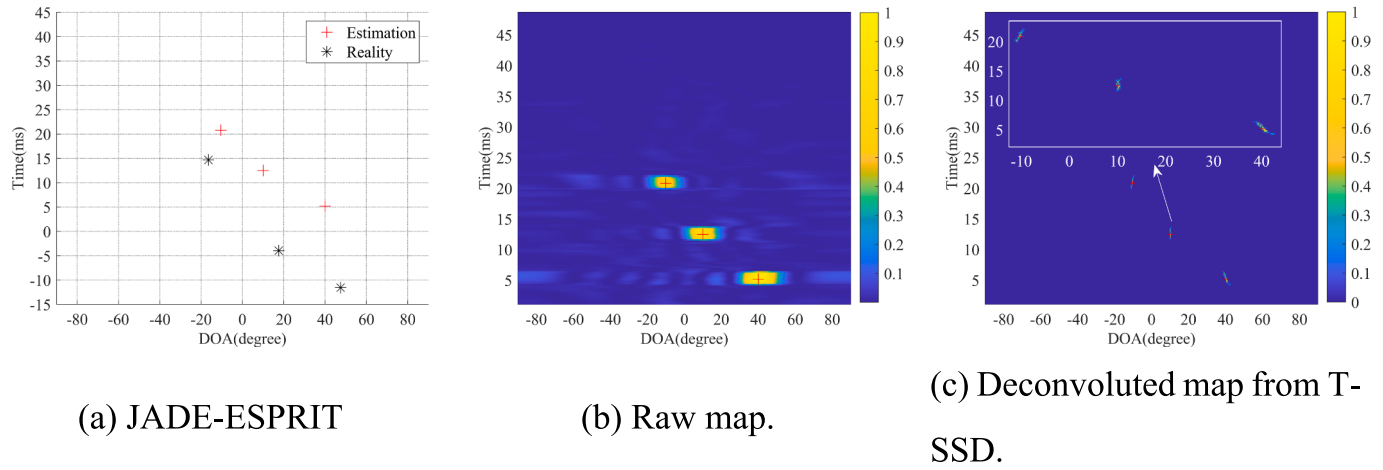


Fig. 5. Distribution of temporal-spatial 2D estimation results at -10 dB .

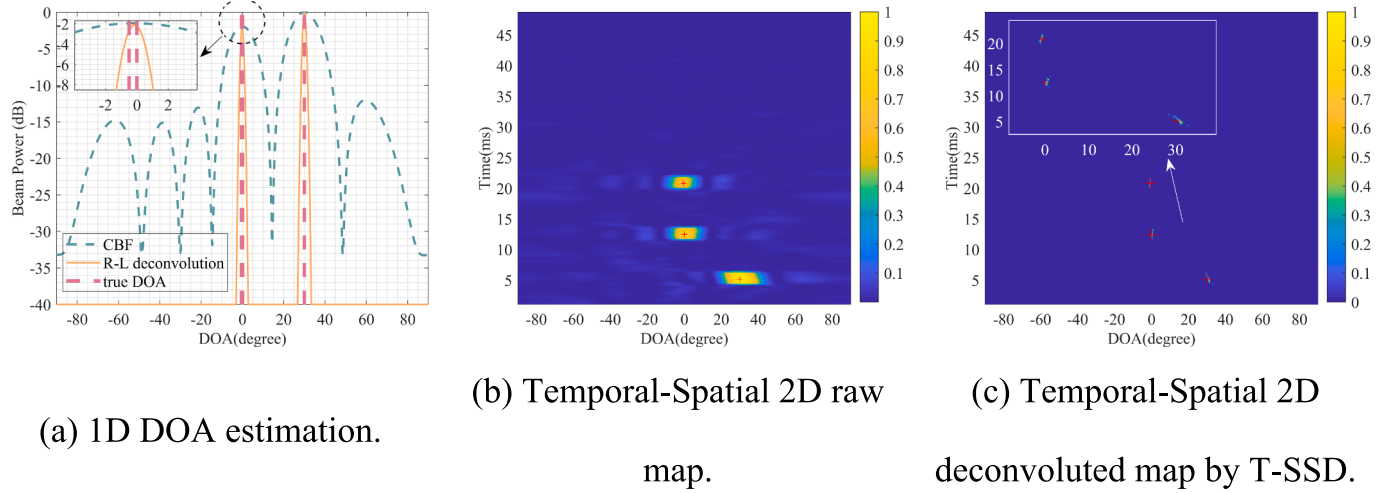


Fig. 6. TOA-DOA measurement results in case 1 (only DOA is close).

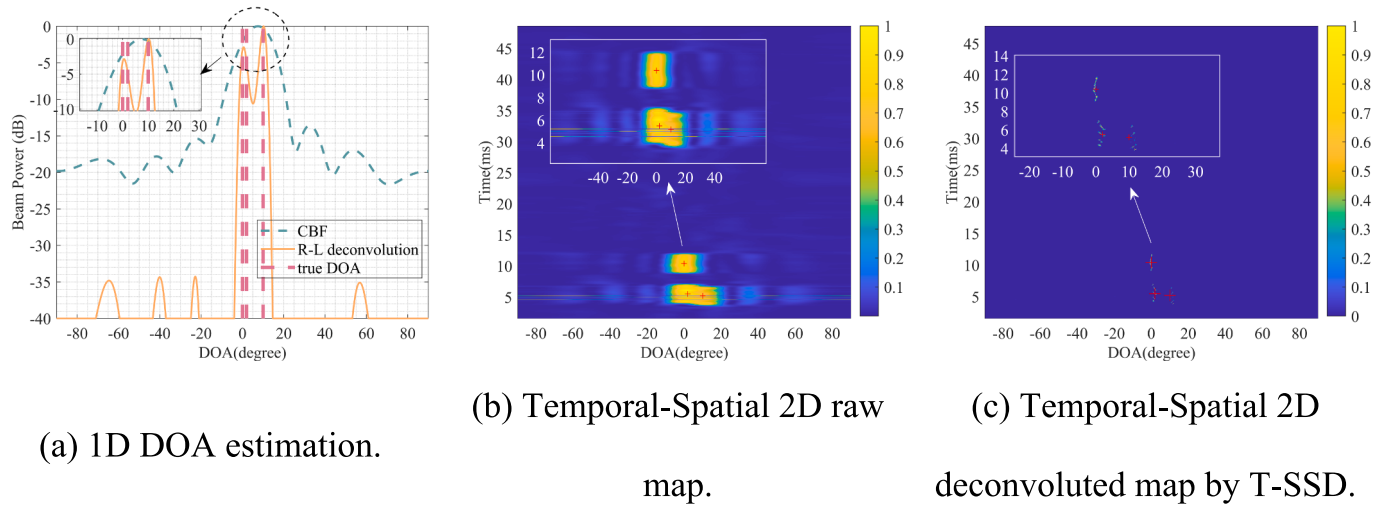


Fig. 7. TOA-DOA measurement results in case 2 (only TOA is close).

4.2. Performance comparison in the case of close TOA/DOA units

In the second simulation, we discuss the case of dense multipath signals coming from very close TOA/DOA units, which is possible for the practical environment.

Case 1: The close case in only DOA units at -10 dB. The signals are from DOA $[30^\circ, 0^\circ, -0.5^\circ]$ and TOA $[5.2 \text{ ms}, 12.5 \text{ ms}, 20.8 \text{ ms}]$. From Fig. 6(a), it can be seen that both the 1D CBF and 1D R-L deconvolution algorithms [24] only distinguish two signals. This is because the two multipath signals with close DOA (0° and -0.5°) fall within the same beam scan. After acquiring the temporal information, the Temporal-Spatial 2D raw map in Fig. 6(b) successfully separates the signals close in DOA. However, Fig. 6(b) shows main-lobe width is nearly 20° in the spatial dimension, which makes it difficult to obtain accurate and reliable DOA estimations. Fig. 6(c) shows the deconvolution result of Fig. 6(b), which proves T-SSD successfully reduce the main-lobe width to $< 1^\circ$ and suppress the side-lobe level to < -40 dB.

Case 2: The close case in only TOA units at -10 dB. Their DOA are $[10^\circ, 2^\circ, 0^\circ]$ and TOA are $[5.2 \text{ ms}, 5.5 \text{ ms}, 10.4 \text{ ms}]$, and the remaining parameter settings are the same as Case 1. As shown in Fig. 7(a), the 1D CBF main-lobe width is about 30° , so all three signals fall into the same beam scan. Although 1D R-L deconvolution algorithm [24] suppresses the main-lobe width and successfully distinguish the signal at 10° , its resolution is insufficient to distinguish signals between 0° and 2° due to dimensional limitations. Fig. 7(b) shows 2D raw map obtained from the joint TOA-DOA estimation model. But the first and second signals are mixed indistinguishably, because their difference in TOA is smaller than the resolution of the conventional cross-correlation algorithm. As shown in Fig. 7(c), T-SSD successfully distinguishes these three signal paths, and the TOA resolution breaks through the limitation of signal bandwidth.

4.3. Resolution performance versus TOA and DOA intervals

In the third simulation, to verify how many TOA/DOA units are needed for T-SSD to distinguish dense multipaths, i.e. the resolution of T-SSD, we set one signal arriving stably at TOA of 0 ms and DOA of 0° . As for the other signal, its TOA varies from 0 ms to 6.67 ms with an interval of 0.67 ms, and DOA varies from 0° to 10° with an interval of 1° . The resolution ability is evaluated by the probability of resolution (POR) expressed as follows:

$$\text{POR} = \frac{O_{\text{success}}}{O_M}, \quad (31)$$

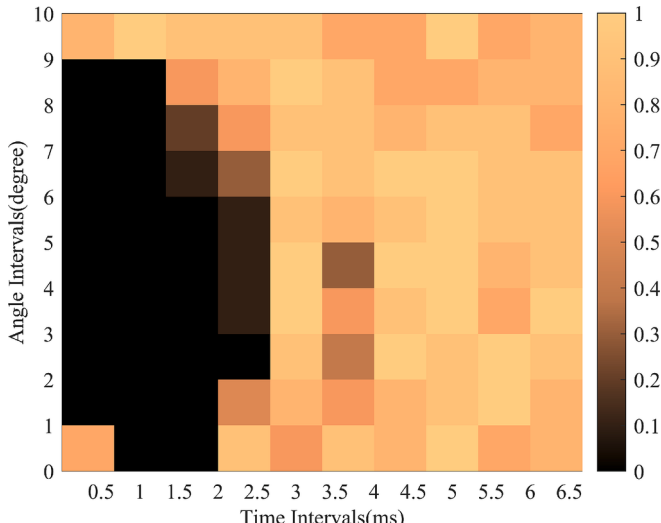


Fig. 8. POR map versus TOA and DOA intervals at -10 dB.

where O_M is the number of tests, and O_{success} is the number of successful estimations. We define that the estimation is successful if the DOA and TOA estimation errors are within 1° and 2 ms respectively.

Fig. 8 shows the POR map versus TOA and DOA intervals at -10 dB. The results indicate that the POR gradually increases with the increase of time and angle intervals. Meanwhile, the larger the time interval, the smaller the angle interval required to achieve stable distinction. When the time interval is higher than 2.5 ms, the T-SSD can distinguish the multipath signals reaching any angular interval. Especially, when the intervals are both 0, these paths are considered as the same and POR = 1. Hence, a bright spot appears in the lower left corner of Fig. 8.

4.4. Performance comparison versus SNR

In the fourth simulation, T-SSD is compared with the JADE-ESPRIT [34], Only-DOA(RL) algorithm in [43] and Only-TOA algorithm in [48] in term of root mean square error (RMSE) at different SNR. The RMSE can be calculated as

$$\text{RMSE} = \sqrt{\frac{1}{O_M L} \sum_{l=1}^L \sum_{o=1}^{O_M} (E_l - \hat{E}_l(o))^2}, \quad (32)$$

where $O_M = 500$ is the number of Monte Carlo experiments, $L = 3$ is the number of multipaths, $\hat{E}_l(o)$ is the DOA and TOA estimation of the l -th signal path at the o -th ($o = 1, 2, \dots, O_M$) experiment. The DOA and TOA setting are the same as in the first simulation, and the SNR varies from -15 dB to 15 dB with 2.5 dB intervals. The CRB given in [49] provides an algorithm-independent benchmark for comparison reference in the RMSE.

The RMSE performance versus SNR in terms of TOA and DOA is shown in Fig. 9. In Fig. 9(a), the RMSE of all the algorithms gradually decreases as the SNR increases. When the SNR is higher than 5 dB, JADE-ESPRIT performs better than Only-DOA(RL) algorithm. However, the JADE-ESPRIT is overly sensitive to noise, resulting in extremely poor estimation reliability at low SNR. Although the Only-DOA(RL) algorithm is insensitive to noise, its RMSE is too large to be practical because of the nonlinear operation in constructing the spectrum convolution response, shown in formula (24). Conversely, the T-SSD shows the lowest RMSE within 2.5° at different SNR close to CRB because of the convolution model without approximation shown in formula (20).

Fig. 9(b) shows the performance of TOA estimation. The sharpness of the cross-correlation function peak increases with SNR, leading to a gradual decrease in the RMSE for Only-TOA and JADE-ESPRIT algorithms. JADE-ESPRIT has a higher RMSE at low SNR but possesses a lower RMSE than the Only-TOA algorithm at 12.5 dB. In comparison, RMSE of T-SSD is very close to CRB at various SNR. Its RMSE remains almost constant because of the SNR gain provided by the cross-correlation process, and the stabilizing effect of regularization techniques, which prevent overfitting to noisy data at the cost of some accuracy. In summary, by coupling temporal and spatial information for joint TOA-DOA estimation, T-SSD shows the best and the most robust performance among the recent algorithms.

4.5. Performance comparison versus element number

In the fifth simulation, we first study the DOA and TOA estimation performance of the T-SSD versus the number of array elements. The number of array elements varies from 3 to 15 at -10 dB, with 500 Monte Carlo experiments conducted for each. And the remaining parameters are the same as the first simulation.

Fig. 10(a) illustrates the RMSE performance versus the element number. As the element number increases from 3 to 8, the RMSE of DOA drops significantly from 13.8° to 0.16° , and then slowly decreases thereafter. Fig. 10(b) shows the estimation distribution versus the elements number, where “o” represents average bias and “-” indicates the

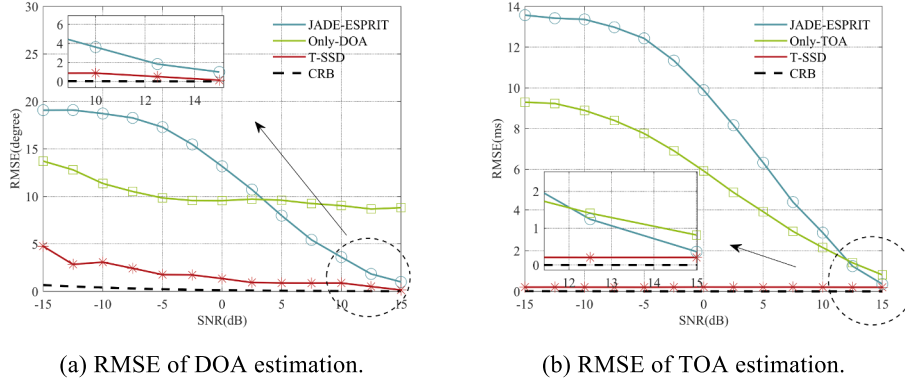


Fig. 9. Performance comparison versus SNR.

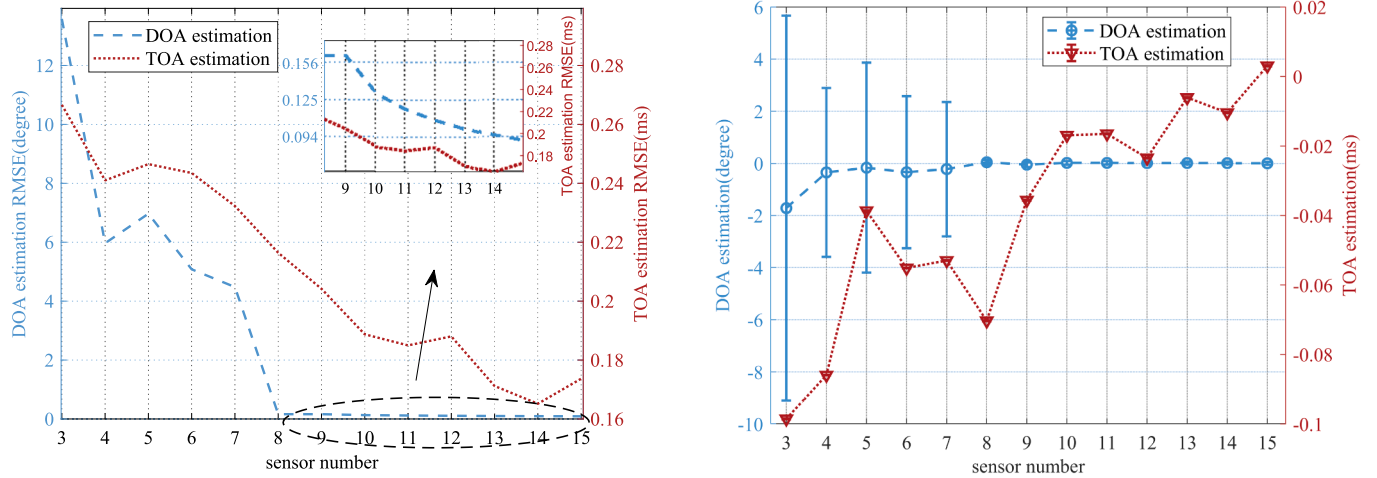


Fig. 10. T-SSD performance versus element number.

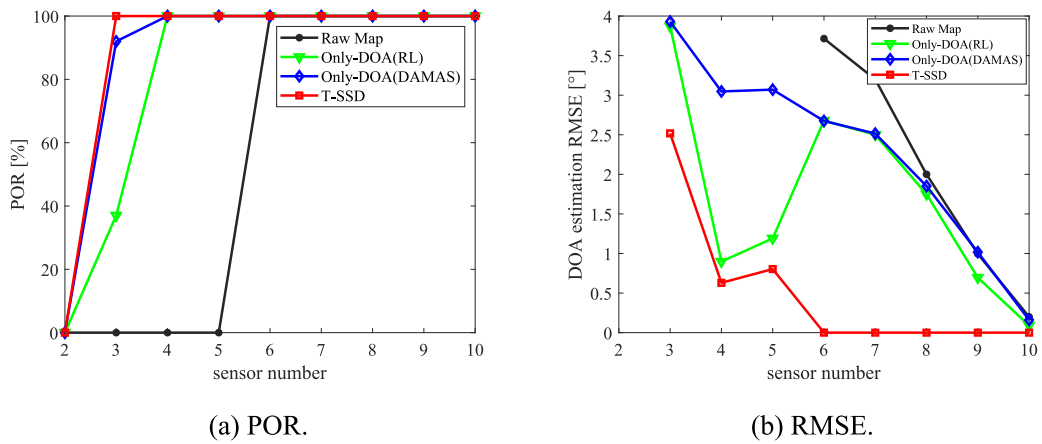


Fig. 11. Algorithm performance versus element number (DOA interval is 20°).

maximum/minimum bias, with the distance between them representing the standard error. Similarly, the DOA distribution exhibits strong fluctuations due to the main-lobe width expanding as array apertures shrink [50]. When the number of array elements exceeds 8, the DOA estimation distribution stabilizes within $\pm 0.15^\circ$, with small fluctuations

not labeled. As for the TOA estimation performance at the same case, its RMSE decreases from 0.265 ms to 0.16 ms and the average bias ranges from -0.1 ms to 0 ms, indicating a system bias during estimation caused by regularization techniques.

And then we conduct a simulation to compare T-SSD, raw map, Only-

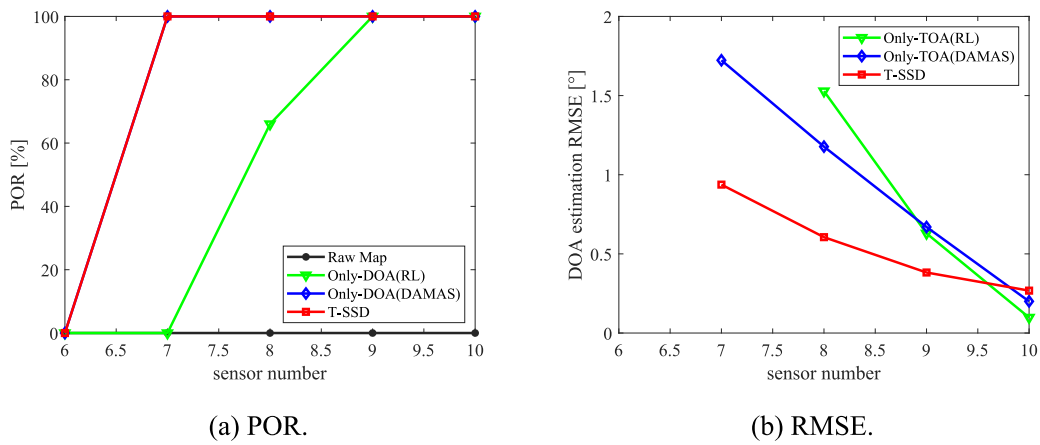


Fig. 12. Algorithm performance versus element number (DOA interval is 10°).

DOA(RL) algorithm in [43], and Only-DOA(DAMAS) algorithm in [51] in terms of POR and RMSE performance versus element number at 0 dB. The angle interval between the two incident signals is 20°, and the time difference is 0 ms. As shown in Fig. 11(a), all the algorithms fail to distinguish multipath signals at the smallest array aperture (only two elements). But T-SSD can achieve the maximum POR with the minimum number of elements among various algorithms. On the premise of successful distinction, Fig. 11(b) shows the RMSE of each algorithm. Note that the RMSE of each algorithm does not strictly decrease with an increasing number of elements. An anomaly occurs when the array has four elements. Although the energy of environmental noise is the same, the multipath signals are coherently superimposed, causing the fourth element's energy to be significantly lower than the others, reducing its SNR and exceeding the algorithm's noise threshold. But the RMSE of T-SSD is always the smallest under various array element numbers.

Finally, we conduct a simulation where the angle interval is set as 10°, and the time difference and SNR are 0 ms and -10 dB. As shown in Fig. 12(a), raw maps cannot distinguish between two signals regardless of the number of elements, and at least 7 array elements are required for the deconvolution algorithm to successfully distinguish multipath signals. Compared to Fig. 11(a), this demonstrates that closer angle intervals result in stronger coherence, requiring more array elements for higher resolution. T-SSD achieves the maximum POR and the lowest RMSE with the fewest elements among various algorithms. Hence, T-SSD can achieve the best and most robust performance, especially with fewer array elements.

4.6. Analysis of computational complexity

By analyzing the processes of various algorithms, we can obtain their computational complexity. Since a computer takes much more burden to process a multiplication or division than an addition or subtraction operation, the computational complexity of the algorithms depends mainly on the number of multiplications and divisions. For the proposed method T-SSD, we can estimate that for each iteration. The number of multiplications is $2N^2$, the number of divisions is $4N$; and the computational complexity for solving the maximum eigenvalue before iteration is N^2 . Hence, the total complexity is $O(4KN^2 + 8KN + 2N^2)$ in complex-valued domain, where N is the number of beams and K is the

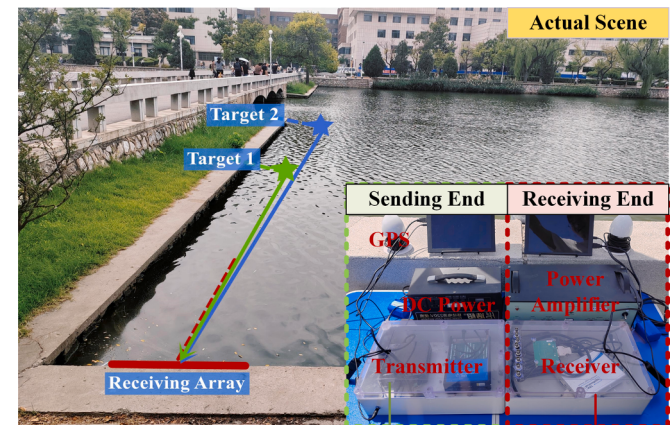


Fig. 13. Experimental scene.

number of iterations. Similarly, the computational complexity of Only-DOA(RL) and Only-DOA(DAMAS) are $O(2KN^2)$ and $O(KN^3 + KN)$, respectively. A smaller N may result in quantization error and yield poor estimation resolution, but a larger N will also require higher computational complexity. The selection of N should be considered as a balance between the angular resolution and computational complexity. In the simulation and experimental process of this paper, we choose $N = 2001$, the angular scanning step is about 0.09°, and the distance resolution error caused by 1 km diagonal distance is 0.15 %, ensuring the resolution capability for practical applications.

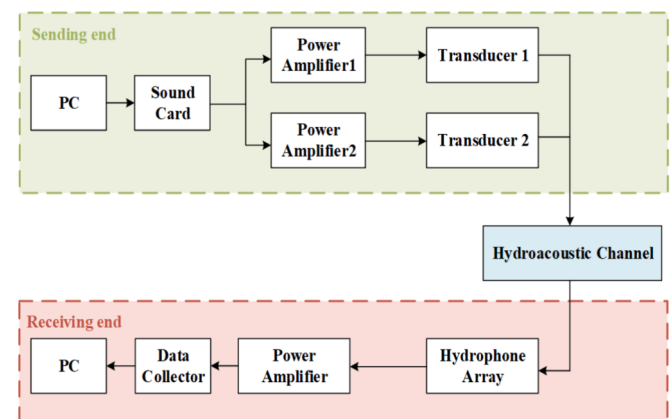


Fig. 14. Diagram of the experiment instruments.

Table 2

Computational complexity analysis.

Algorithms	Complexity	computation time
Only-DOA(RL)	$O(2KN^2)$	1.93 s
Only-DOA(DAMAS)	$O(KN^3 + KN)$	40.25 s
Proposed T-SSD	$O(4KN^2 + 8KN + 2N^2)$	4.19 s

Table 2 summarizes the main computational complexity and computation time of these algorithms. The complexity of T-SSD is significantly lower than DAMAS, but still twice as high as R-L.

5. Experiment

5.1. Experimental setup

To validate the performance of T-SSD, experiments were conducted at Jingye Lake in Tianjin, China. After the hydrologic exploration using the Valeport miniSVP, the average depth of the lake was determined to be approximately 5 m, and the speed of sound was 1476 m/s. The experimental scene is depicted in Fig. 13. To ensure the received signals are coherent, two identical transducers with type of 715-CT-22 send the same source signal. The hydrophone array consists of seven Brüel & Kjær 8104 hydrophones with an array spacing of 0.05 m.

Both the array and the transducers are placed at 1.5 m depth, and the hydrophone array is placed horizontally to avoid receiving unknown multipath signals from seafloor and surface as much as possible. Measured by the NTS-382R6 total station, one transducer labelled as Target 1 is placed at -4.03° and 11.52 m from the array, and the other labelled as Target 2 is placed at -3.03° and 21.03 m from the array, so that the far-field conditions are satisfied[52]. The source signal is 13–17 kHz LFM with a duration of 50 ms. At the receiving array, the sampling rate is 200 kHz, and the received signal is processed by a filter with a passband of 10–20 kHz, and a gain of 6.7 dB. The detailed diagram of the experimental instruments is shown in Fig. 14.

5.2. Joint TOA-DOA estimation performance in the lake

Fig. 15(a)(b) illustrates that the estimation results of these two targets in 1D spatial spectrograms. It is evident that the T-SSD algorithm provides the most accurate angle estimation, the narrowest main-lobe width, and the lowest side-lobe height. Fig. 15(d) shows that JADE-ESPRIT successfully estimates the DOA and TOA of these two targets.

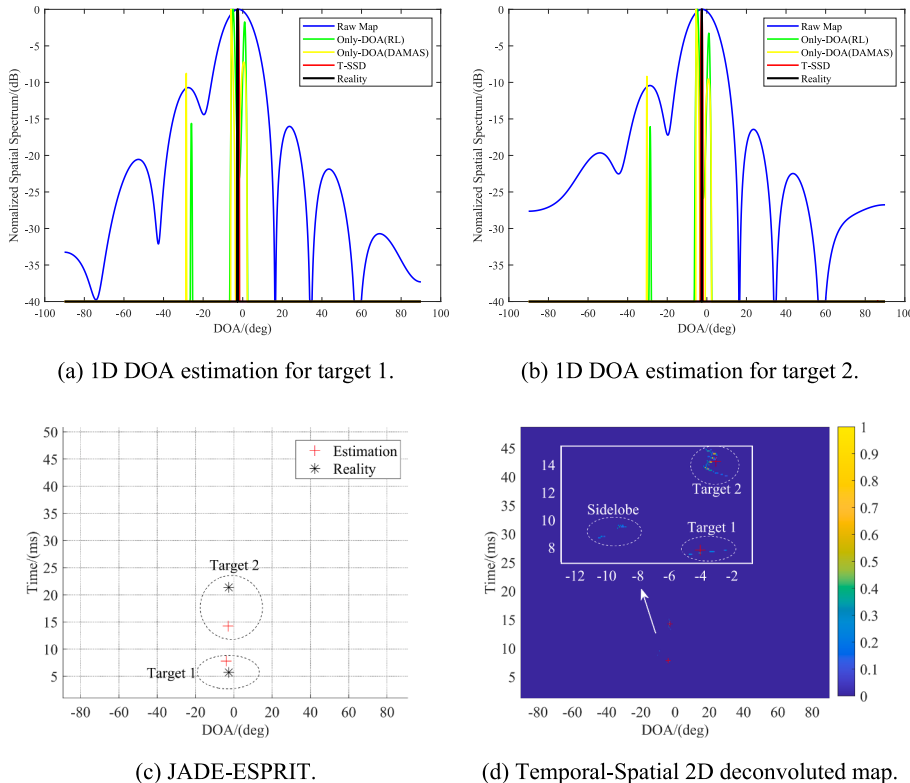


Fig. 15. Estimation results of the coherent signal by different methods.

Table 3
Rmse Of Jade-Esprit And T-Ssd.

Algorithms	DOA RMSE	TOA RMSE
JADE-ESPRIT	1.05°	5.24 ms
T-SSD	0.29°	0.20 ms

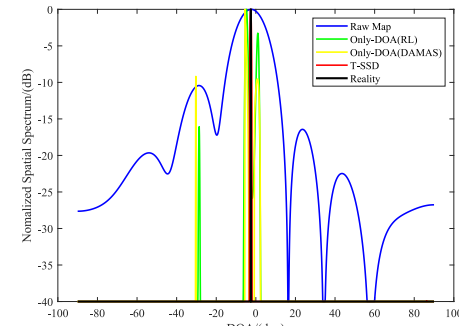
However, JADE-ESPRIT requires the number of sources to be known, which is difficult to acquire in practice. After providing posterior information about source number to JADE-ESPRIT, we can only estimate the two pairs of DOA and TOA in line-of-sight. And we miss the other non-line-of-sight multipath information, making the estimation results of JADE-ESPRIT biased. Fig. 15(d) shows the estimation results of T-SSD, the true values are marked with red cross symbols. T-SSD not only estimates the line-of-sight DOA and TOA information of the two targets but also successfully estimates the non-line-of-sight signals, which is favorable for further analysis and judgment of the target locations.

Table 3 shows the RMSE of the target estimation results of JADE-ESPRIT and T-SSD. The resolution performance of T-SSD is obviously better than that of JADE-ESPRIT.

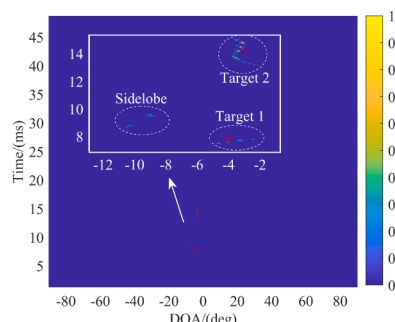
6. Conclusion

In order to estimate DOA of wideband signals in the multipath-rich environment, a temporal-spatial two-dimensional sparse deconvolution joint estimation algorithm (T-SSD) is proposed in this paper. The first contribution is to apply cross-correlation function in the construction of a joint TOA-DOA estimation model, which not only couples the temporal parameters into the spatial estimation model but also maximizes the output SNR and enhances the robustness of the algorithm. The second contribution is to post-process this joint model by using the sparse characteristic of channel in the temporal-spatial domain to suppress the main-lobe width and the side-lobe level to obtain high-resolution estimation results.

The numerical simulations show the T-SSD algorithm in DOA



(b) 1D DOA estimation for target 2.



(d) Temporal-Spatial 2D deconvoluted map.

estimation is an unbiased estimator with small variance close to CRB at -15 dB SNR with only 8 array elements. The underwater experiment demonstrates the DOA resolution of T-SSD is as low as 0.3° . The analysis of computational complexity indicates that the complexity of T-SSD is significantly lower than DAMAS, but still twice as high as R-L. When applying T-SSD to real-time applications, such as sound source localization, multipath signal identification, target detection, we consider combining it with fast algorithms to reduce computational complexity in future work.

Credit Authorship Statement.

Quan Tao: Conceptualization, Methodology, Writing – original draft. **Jingjing Fan:** Formal analysis, Supervision, Funding acquisition. **Zhiwen Qian:** Conceptualization, Visualization. **Xiaomei Fu:** Data curation, Validation, Funding acquisition, Writing – review & editing.

CRediT authorship contribution statement

Quan Tao: Writing – original draft, Methodology. **Jingjing Fan:**

Appendix A

First, let z_0 be the power of Gaussian white noise in the received signal model, $s(f)$ and $\mathbf{X}(f)$ be the spectral density functions of the transmitted and received signals, respectively. Then, the cross-correlation function (8) can be expressed as:

$$R_{xs}(t) = \int_{-\infty}^{+\infty} \mathbf{X}(f) s^*(f) e^{j2\pi ft} df \quad (A1)$$

The output noise power after cross-correlation with the source signal can be expressed as:

$$Z_0 = z_0 \int_{-\infty}^{+\infty} |s^*(f)|^2 df \quad (A2)$$

Therefore, the ratio of the instantaneous power of the output signal to the average power of the noise at the moment of t_0 sampling-point is:

$$SNR_{cross} = \frac{\left| \int_{-\infty}^{+\infty} \mathbf{X}(f) s^*(f) e^{j2\pi f t_0} df \right|^2}{z_0 \int_{-\infty}^{+\infty} |s^*(f)|^2 df} \quad (A3)$$

According to the Schwarz inequality:

$$\left| \int_{-\infty}^{+\infty} g_1(a) g_2(a) da \right|^2 \leq \int_{-\infty}^{+\infty} |g_1(a)|^2 df \int_{-\infty}^{+\infty} |g_2(a)|^2 df \quad (A4)$$

The inequality takes its maximum value when and only when $g_1(a) = \xi g_2^*(a)$, where ξ is an arbitrary constant. If we let $g_1(a) = \mathbf{X}(f) e^{j2\pi f t_0}$, then we get:

$$\begin{aligned} SNR_{cross} &\leq \frac{\int_{-\infty}^{+\infty} |\mathbf{X}(f) e^{j2\pi f t_0}|^2 df \int_{-\infty}^{+\infty} |s^*(f)|^2 df}{z_0 \int_{-\infty}^{+\infty} |s^*(f)|^2 df} \\ &= \frac{\int_{-\infty}^{+\infty} |\mathbf{X}(f) e^{j2\pi f t_0}|^2 df}{z_0} \end{aligned} \quad (A5)$$

The inequality takes its maximum value when and only when $\mathbf{X}(f) = \xi s(f) e^{-j2\pi f t_0}$, taking an inverse Fourier transform of it:

$$\mathbf{X}(t) = \xi s(t - t_0) \quad (A6)$$

The equation can be satisfied when $\xi = \beta$ and $t_0 = T$. Where $\beta = [\beta_1, \dots, \beta_L]^T$ and $T = [t_1, \dots, t_L]^T$ are the attenuation and delay parameters of the multipath channel, respectively. It can be proved that cross-correlation can maximize the output SNR. 公式节(下一节).

Appendix B

Assuming the source signal is not LFM but a more general broadband signal, the correlation-covariance result is not a simple wave with frequency f_c^l but with multiple frequencies. Hence, it is necessary to converge these frequencies onto a reference frequency through matrix transformation before performing CBF. The reference frequency is typically chosen as the center frequency.

The key to the matrix transformation is to construct a focusing transformation matrix $\mathbf{T}(f_j)$ such that:

$$\min_{\mathbf{T}(f_j)} \left\| \mathbf{U}_S(f_0) - \mathbf{T}(f_j) \mathbf{U}_S(f_j) \right\|_F^2 \quad (B1)$$

where $\mathbf{U}_S(f_0)$ is the signal subspace eigenvector matrix at the reference frequency f_0 and $\mathbf{U}_S(f_j)$ is the eigenvector matrix at the frequency f_j , obtained

from the eigen decomposition of the correlation-covariance matrix.

The eigenvectors corresponding to the first L_p largest eigenvalues of the covariance matrix are similar to the steering vector $\nu_r = [\nu_{r1}, \dots, \nu_{rm}, \dots, \nu_{rM}]^T$:

$$\text{span}\{u_1, u_2, \dots, u_{L_p}\} = \text{span}\{\nu_1, \nu_2, \dots, \nu_{L_p}\} \quad (\text{B2})$$

where $\text{span}\{\bullet\}$ denotes the vector space.

By applying eigen decomposition, the correlation-covariance matrix at f_j frequency $\mathbf{R}(f_j)$ can be expressed as:

$$\mathbf{R}(f_j) = \mathbf{U}(f_j)\eta(f_j)\mathbf{U}^H(f_j) \quad (\text{B3})$$

where $\mathbf{U}(f_j)$ is the $M \times M$ eigenvector matrix of $\mathbf{R}(f_j)$, $\eta(f_j) = \text{diag}(\delta_{11}, \delta_{22}, \dots, \delta_{MM})$ is the eigenvalue matrix, and δ_{ii} is the eigenvalues of the cross-covariance $\mathbf{R}(f_j)$. We can get: $\delta_{11} \geq \delta_{22} \geq \dots \geq \delta_{L_p L_p} > \delta_{L_p+1, L_p+1} \dots \geq \delta_{MM}$.

We define the eigenvector $\mathbf{U}_s(f_j)$ is the $M \times L_p$ matrix corresponding to the first L_p largest eigenvalues of the eigenvalue matrix $\eta(f_j)$ so that the rank of $\mathbf{U}_s(f_j)$ is L_p . L_p is the number of signals in the p -th time-domain sliding window, generally $L_p = 1$. 公式节 (下一节).

Appendix C

The FSS algorithm [53] proves that $\mathbf{T}(f_j)$ is a Hermitian matrix and gives the expression under the Frobenius norm constrain:

$$\mathbf{T}(f_j) = \mathbf{U}\mathbf{V}^H \quad (\text{C1})$$

where \mathbf{U} and \mathbf{V} are the left and right singular matrices of the matrix $\mathbf{C} = \mathbf{U}_s(f_0)\mathbf{U}_s^H(f_j)$.

It is noticeable that, $\mathbf{T}(f_j)$ is a Hermitian matrix that matches $\mathbf{T}^H(f_j)\mathbf{T}(f_j) = I$. To construct the focusing matrix, we can rewrite (B1) as follows:

$$\begin{aligned} & \left\| \mathbf{U}_s(f_0) - \mathbf{T}(f_j)\mathbf{U}_s(f_j) \right\|_F^2 \\ &= \text{tr} \left([\mathbf{U}_s(f_0) - \mathbf{T}(f_j)\mathbf{U}_s(f_j)] [\mathbf{U}_s(f_0) - \mathbf{T}(f_j)\mathbf{U}_s(f_j)]^H \right) \\ &= \text{tr}(\mathbf{U}_s(f_0)\mathbf{U}_s^H(f_0)) + \text{tr}(\mathbf{U}_s(f_j)\mathbf{U}_s^H(f_j)) \\ &\quad - 2\text{Re}[\text{tr}(\mathbf{U}_s(f_0)\mathbf{U}_s^H(f_j)\mathbf{T}^H(f_j))] \end{aligned} \quad (\text{C2})$$

Obviously, the first two terms in (C2) are fixed values, and to minimize this function, the last term needs to take the maximum value. Let the matrix \mathbf{C} be:

$$\mathbf{C} = \mathbf{U}_s(f_0)\mathbf{U}_s^H(f_j) \quad (\text{C3})$$

By decomposing the matrix with singular values, the matrix is given by:

$$\mathbf{C} = \mathbf{U} \sum \mathbf{V}^H \quad (\text{C4})$$

Where \mathbf{U} and \mathbf{V} are the left and right singular matrices of the matrix \mathbf{C} . $\sum = \text{diag}(\sigma_{11}, \sigma_{22}, \dots, \sigma_{MM})$, σ_{ii} denotes the singular value of the matrix \mathbf{C} .

Assuming the rank of the matrix \mathbf{C} is r , we can get: $\sigma_{11} \geq \sigma_{22} \geq \dots \geq \sigma_{rr} > \sigma_{r+1, r+1} = \dots = \sigma_{MM} = 0$.

Then, the last term of (C2) can be written as:

$$\begin{aligned} & \text{Re}[\text{tr}(\mathbf{U}_s(f_0)\mathbf{U}_s^H(f_j)\mathbf{T}^H(f_j))] \\ & \leq |\text{tr}(\mathbf{U}_s(f_0)\mathbf{U}_s^H(f_j)\mathbf{T}^H(f_j))| \\ &= |\text{tr}(\mathbf{U} \sum \mathbf{V}^H \mathbf{T}^H(f_j))| \\ &= |\text{tr}(\sum \mathbf{V}^H \mathbf{T}^H(f_j) \mathbf{U})| \end{aligned} \quad (\text{C5})$$

Since $\mathbf{Z} = \mathbf{V}^H \mathbf{T}^H(f_j) \mathbf{U}$ is a unitary matrix, (C5) takes its maximum value when $|\mathbf{Z}_{ii}| = 1$, $i = 1, 2, \dots, M$, at which the focusing matrix can be considered as: $\mathbf{T}(f_j) = \mathbf{U}\mathbf{V}^H$.

The correlation-covariance matrix can be approximated to the narrowband case based on the focusing transformation matrix:

$$\mathbf{R}_{\text{narrow}} = \frac{1}{J} \sum_{j=1}^J \mathbf{T}(f_j) \mathbf{R}(f_j) \mathbf{T}^H(f_j) \quad (\text{C6})$$

where J is the number of frequency points, and we define it is the same as the number of sampling points in the time domain in this paper. $\mathbf{R}(f_j)$ is the correlation-covariance matrix at f_j frequency.

Appendix D. Supplementary data

Supplementary data to this article can be found online at <https://doi.org/10.1016/j.measurement.2025.117330>.

Data availability

Data will be made available on request.

References

- [1] M. Alibakhshikenari, et al., Study on on-chip antenna design based on metamaterial-inspired and substrate-integrated waveguide properties for millimetre-wave and THz integrated-circuit applications, *Journal of Infrared, Millimeter, and Terahertz Waves* 42 (1) (2021) 17–28, <https://doi.org/10.1007/s10762-020-00753-8>.
- [2] M. Alibakhshikenari, et al., Bandwidth and gain enhancement of composite right left handed metamaterial transmission line planar antenna employing a non foster impedance matching circuit board, *Sci. Rep.* 11 (1) (2021) 7472, <https://doi.org/10.1038/s41598-021-86973-x>.
- [3] M. Alibakhshikenari, B. S. Virdee, A. A. Althuwayb, D. Mariyanayagam, and E. Limiti, “Compact and Low-Profile On-Chip Antenna Using Underside Electromagnetic Coupling Mechanism for Terahertz Front-End Transceivers,” *Electronics*, vol. 10, no. 11, doi: 10.3390/electronics1011264.
- [4] M. Alibakhshikenari, et al., Dual-Polarized Highly Folded Bowtie Antenna With Slotted Self-Grounded Structure for Sub-6 GHz 5G Applications, *IEEE Trans. Antennas Propag.* 70 (4) (2022) 3028–3033, <https://doi.org/10.1109/TAP.2021.3118784>.
- [5] M. Alibakhshikenari, et al., Broadband 3-D shared aperture high isolation nine-element antenna array for on-demand millimeter-wave 5G applications, *Optik* 267 (2022) 169708, <https://doi.org/10.1016/j.jleo.2022.169708>.
- [6] B. Zhang, X. Hou, Y. Yang, L. Yang, Y. Wang, A fast variational bayesian adaptive extended kalman filter for robust underwater direction-of-arrival tracking, *IEEE Sens. J.* 23 (13) (2023) 14709–14720, <https://doi.org/10.1109/JSEN.2023.3275318>.
- [7] H. H. Chen, J. Y. Zhang, B. Jiang, X. R. Cui, R. R. Zhou, and Y. C. Zhang, “Multi-source underwater DOA estimation using PSO-BP neural network based on high-order cumulant optimization,” (in English), *CHINA COMMUNICATIONS*, 2023 MAY 10 2023, doi: 10.23919/JCC.ea.2021-0031.202302.
- [8] B. Qi, DOA estimation of the coherent signals using beampspace matrix reconstruction, *Signal Process.* 191 (2022) 108349, <https://doi.org/10.1016/j.sigpro.2021.108349>.
- [9] L. Cheng, Y. Li, L. Zou, Y. Qin, DOA estimation for highly correlated and coherent multipath signals with Ultralow SNRs, *International Journal of Antennas and Propagation* 2019 (2019) 2837315, <https://doi.org/10.1155/2019/2837315>.
- [10] Z. Xu, H. Li, K. Yang, A Modified Differential Beamforming and Its Application for DOA Estimation of Low Frequency Underwater Signal, *IEEE Sens. J.* 20 (16) (2020) 8890–8902, <https://doi.org/10.1109/JSEN.2020.2988025>.
- [11] C. Yang, Y. Wang, Y. Wang, D. Y. Hu, and H. Guo, “An improved functional beamforming algorithm for far-field multi-sound source localization based on Hilbert curve,” (in English), *APPLIED ACOUSTICS*, vol. 192, APR 2022, Art no. 108729, doi: 10.1016/j.apacoust.2022.108729.
- [12] M.M. Fakharian, M. Alibakhshikenari, C.H. See, R. Abd-Alhameed, A high gain multiband offset MIMO antenna based on a planar log-periodic array for Ku/K-band applications, *Sci. Rep.* 12 (1) (2022) 4044, <https://doi.org/10.1038/s41598-022-07866-1>.
- [13] M. Alibakhshikenari, et al., Singular Integral Formulations for Electrodynamic Analysis of Metamaterial-Inspired Antenna Array, *IEEE Antennas Wirel. Propag. Lett.* 20 (2) (2021) 179–183, <https://doi.org/10.1109/LAWP.2020.3043380>.
- [14] M. Alibakhshikenari, et al., Novel Concentric Hexagonal-Shaped RFID Tag Antenna With T-Shaped Stub Matching, *IEEE Journal of Radio Frequency Identification* 6 (2022) 112–120, <https://doi.org/10.1109/JRFID.2021.3124966>.
- [15] T. F. Brooks and W. M. Humphreys, “A deconvolution approach for the mapping of acoustic sources (DAMAS) determined from phased microphone arrays,” (in English), *JOURNAL OF SOUND AND VIBRATION*, vol. 294, no. 4-5, pp. 856–879, JUL 25 2006, doi: 10.1016/j.jsv.2005.12.046.
- [16] W.H. Richardson, Bayesian-based iterative method of image restoration*, *J. Opt. Soc. Am.*, 62 (1) (1972) 55–59, <https://doi.org/10.1364/JOSA.62.000055>.
- [17] J.A. Hogbom, Aperture synthesis with a non-regular distribution of interferometer baselines, *Astronomy Astrophys Suppl* 15 (1974) 417.
- [18] K. Moszyński, Solving least squares problems, *Solving Least Squares Problems* (1983).
- [19] A. Beck and M. Teboulle, “A fast Iterative Shrinkage-Thresholding Algorithm with application to wavelet-based image deblurring,” in *2009 IEEE International Conference on Acoustics, Speech and Signal Processing*, 19–24 April 2009 2009, pp. 693–696, doi: 10.1109/ICASSP.2009.4959678.
- [20] R.P. Dougherty, Extensions of DAMAS and benefits and limitations of deconvolution in beamforming, *Aiaa/ceas Aeroacoustics Conference* (2013).
- [21] K. Ehrenfried and L. Koop, “Comparison of iterative deconvolution algorithms for the mapping of acoustic sources,” (in English), *AIAA JOURNAL*, vol. 45, no. 7, pp. 1584–1595, JUL 2007, doi: 10.2514/1.26320.
- [22] O. Lylloff, E. Fernández-Grande, F. Agerkvist, J. Hald, E.T. Roig, M.S. Andersen, Improving the efficiency of deconvolution algorithms for sound source localization, *J. Acoust. Soc. Am.* 138 (1) (2015) 172–180.
- [23] L. Shen, Z. Chu, L. Tan, D. Chen, F. Ye, Improving the sound source identification performance of sparsity constrained deconvolution beamforming utilizing SFISTA, *Shock Vib.* 2020 (7) (2020) 1–9.
- [24] T.C. Yang, Deconvolved conventional beamforming for a horizontal line array, *IEEE J. Ocean Eng.* 43 (1) (2018) 160–172, <https://doi.org/10.1109/JOE.2017.2680818>.
- [25] Z. Chu, Y. Yang, Comparison of deconvolution methods for the visualization of acoustic sources based on cross-spectral imaging function beamforming, *Mech. Syst. Sig. Process.* 48 (1) (2014) 404–422, <https://doi.org/10.1016/j.ymssp.2014.03.012>.
- [26] T. F. Brooks and W. M. Humphreys, Jr, “Extension of DAMAS Phased Array Processing for Spatial Coherence Determination (DAMAS-C),” in *12th AIAA/CEAS Aeroacoustics Conference, Cambridge, Massachusetts, May 8-10, 2006*, 2006.
- [27] X.U. Liang, A fast deconvolution approach for the mapping of coherent acoustic sources, *Journal of Mechanical Engineering* 54 (23) (2018) 82.
- [28] F. Wang, X. Tian, X. Liu, B. Gu, F. Zhou, Y. Chen, Combination Complex-Valued Bayesian Compressive Sensing Method for Sparsity Constrained Deconvolution Beamforming, *IEEE Trans. Instrum. Meas.* 71 (2022) 1–13, <https://doi.org/10.1109/TIM.2022.3169537>.
- [29] S. Ma and T. C. Yang, “The Effect of Elevation Angle on Bearing Estimation for Array Beamforming in Shallow Water,” in *Global Oceans 2020: Singapore – U.S. Gulf Coast*, 5–30 Oct. 2020 2020, pp. 1–5, doi: 10.1109/IEECONF38699.2020.9389083.
- [30] R. Zhao, M. Khalid, O.A. Dobre, X. Wang, Physical Layer Node Authentication in Underwater Acoustic Sensor Networks Using Time-Reversal, *IEEE Sens. J.* 22 (4) (2022) 3796–3809, <https://doi.org/10.1109/JSEN.2022.3142160>.
- [31] M. Wax, A. Leshem, Joint estimation of time delays and directions of arrival of multiple reflections of a known signal, *IEEE Trans. Signal Process.* 45 (10) (1997) 2477–2484, <https://doi.org/10.1109/78.640713>.
- [32] M. Feder, E. Weinstein, Parameter estimation of superimposed signals using the EM algorithm, *IEEE Trans. Acoust. Speech Signal Process.* 36 (4) (1988) 477–489, <https://doi.org/10.1109/29.1552>.
- [33] B.H. Fleury, M. Tschudin, R. Heddergott, D. Dahlhaus, K.I. Pedersen, Channel parameter estimation in mobile radio environments using the SAGE algorithm, *IEEE J. Sel. Areas Commun.* 17 (3) (1999) 434–450, <https://doi.org/10.1109/49.753729>.
- [34] M. C. Vanderveen, A. J. V. d. Veen, and A. Paulraj, “Estimation of multipath parameters in wireless communications,” *IEEE Transactions on Signal Processing*, vol. 46, no. 3, pp. 682–690, 1998, doi: 10.1109/78.661335.
- [35] X. Li, W. Cui, H. Xu, B. Ba, Y. Zhang, A Novel Method for DOA and Time Delay Joint Estimation in Multipath OFDM Environment, *International Journal of Antennas and Propagation* 2020 (2020) 3952175, <https://doi.org/10.1155/2020/3952175>.
- [36] B.G. Katsnelson, B.G. Пётников, J. Lynch, Fundamentals of shallow water acoustics, *Fundamentals of Shallow Water Acoustics* (2012).
- [37] F. Jensen, “Numerical Models of Sound Propagation in Real Oceans,” in *OCEANS 82*, 20–22 Sept. 1982 1982, pp. 147–154, doi: 10.1109/OCEANS.1982.1151749.
- [38] W.-J. Zeng, X. Jiang, X.-L. Li, X.-D. Zhang, Deconvolution of sparse underwater acoustic multipath channel with a large time-delay spread, *J. Acoust. Soc. Am.* 127 (2) (2010) 909–919, <https://doi.org/10.1121/1.3278604>.
- [39] H. Wang, J. Tang, F. Zhang, Design of special structure FIR filters and two-channel quadrature mirror FIR filter bank with sparse coefficients, *Digital Signal Process.* 133 (2023) 103843, <https://doi.org/10.1016/j.dsp.2022.103843>.
- [40] Q. Song, X. Ma, High-resolution time delay estimation algorithms through cross-correlation post-processing, *IEEE Signal Process. Lett.* 28 (2021) 479–483, <https://doi.org/10.1109/LSP.2020.3048843>.
- [41] X. Li and X. C. A. Ma, “Joint Doppler shift and time delay estimation by deconvolution of generalized matched filter,” (in English), *EURASIP JOURNAL ON ADVANCES IN SIGNAL PROCESSING*, vol. 2021, no. 1, JUN 22 2021, Art no. 29, doi: 10.1186/s13634-021-00741-7.
- [42] L. Qu, Sparse Blind Deconvolution Method for Wall Parameters Estimation, *IEEE Geosci. Remote Sens. Lett.* 19 (2022) 1–5, <https://doi.org/10.1109/LGRS.2020.3029082>.
- [43] C. Ma, D. Sun, J. Mei, and T. Teng, “Spatiotemporal two-dimensional deconvolution beam imaging technology,” *Applied Acoustics*, vol. 183.
- [44] M. Wu, C. Hao, Super-Resolution TOA and AOA Estimation for OFDM Radar Systems Based on Compressed Sensing, *IEEE Trans. Aerosp. Electron. Syst.* 58 (6) (2022) 5730–5740, <https://doi.org/10.1109/TAES.2022.3178393>.
- [45] M. Donatelli and L. Reichel, “Square smoothing regularization matrices with accurate boundary conditions,” (in English), *JOURNAL OF COMPUTATIONAL AND APPLIED MATHEMATICS*, vol. 272, pp. 334–349, DEC 15 2014, doi: 10.1016/j.cam.2013.08.015.
- [46] G. H. Golub and C. F. Van Loan, *Matrix computations* (3rd ed.). Matrix computations (3rd ed.), 1996.
- [47] W. Zhao, et al., Enhanced detection of fluorescence fluctuations for high-throughput super-resolution imaging, *Nat. Photonics* 17 (9) (2023) 806–813, <https://doi.org/10.1038/s41566-023-01234-9>.

- [48] J. Ianniello, Time delay estimation via cross-correlation in the presence of large estimation errors, *IEEE Trans. Acoust. Speech Signal Process.* 30 (6) (1982) 998–1003, <https://doi.org/10.1109/TASSP.1982.1163992>.
- [49] F. Wen, P. Liu, H. Wei, and Y. Zhang, “Benefit of Joint DOA and Delay Estimation with Application to Indoor Localization in WiFi and 5G,” ed, 2018.
- [50] Q. Yang and Y. Liu, “Research on DOA Technology of Small Aperture Array Based on Compressed Sensing,” in *2019 International Symposium on Antennas and Propagation (ISAP)*, 27-30 Oct. 2019 2019, pp. 1-4.
- [51] H. Baali, A. Bouzerdoum, and A. Khelif, “Sparsity And Nonnegativity Constrained Krylov Approach For Direction Of Arrival Estimation,” *IEEE*, 2021.
- [52] J. J. Handfield, R.M. Rao, S. A. Dianat, “Near-field MVDR source localization,” presented at the WIRELESS SENSING AND PROCESSING III, 2008.
- [53] F. Ma, X. Zhang, Wideband DOA estimation based on focusing signal subspace, *SIViP* 13 (4) (2019) 675–682, <https://doi.org/10.1007/s11760-018-1396-4>.